Supplement to the paper "Singular modes of the Rayleigh instability in three-dimensional streamwise-vortex flows" by S.N.Timoshin & F.T.Smith.

This is an extended version of section 4 of the paper containing a more detailed analysis of the three model examples of the vortex flow.

4. Some specific examples.

Given the vortex curvature distribution K_1, solution of the amplitude equation (3.8) of the previous section becomes a more or less routine computational task, the matter being somewhat complicated by the fact that the wave parameters $\tilde{\alpha}, \tilde{c}$ enter the equation in a non-straightforward manner involving, most crucially, integral properties of the vortex as a whole and also, in the case of neutral disturbances, local curvature at the critical level, on account of (3.9). This section presents three examples of computations and analysis in model vortex flows with significantly different properties of the curvature. Attention will mostly be paid to the changes in wave characteristics caused by variations in the spanwise period of the flow, and to possible deviations from the short-/long-scale limit properties described in section 3. In all the cases below the vortex field is assumed to be symmetric with respect to the origin in ζ so that the relevant wave modes can be divided into families of even and odd solutions. For brevity only, the results are presented for the even family; properties of the odd modes examined on several occasions were found to be similar.

In order to illustrate the possibility of a continuous connection between the large- and small-$\tilde{\beta}$ limit solutions introduced earlier in section 3, for our *first example* we take a smooth curvature distribution, namely

$$K_1(Y,\zeta) = (\mu + \nu \cos \zeta)(1 + Y^2)^{-1}, \qquad (4.1)$$

with constants μ, ν. The equation (3.8) then acquires the form

$$\tilde{\beta}^2 A_{\zeta\zeta} + (S_1 + S_2 \cos \zeta)A = 0, \qquad (4.2)$$

where

$$S_1 = \tilde{\alpha} + (s_1 + is_2)\tilde{c} - \mu\pi s_3(\tilde{c} + i)^{-1}, S_2 = -\nu\pi s_3(\tilde{c} + i)^{-1}. \qquad (4.3)$$

Solutions of (4.2) satisfying the periodicity conditions $A(0) = A(2\pi), A'(0) = A'(2\pi)$ were obtained numerically using a second-order accurate finite-difference approximation for the equation with the explicit normalization $A(0) = 1$ in the case of even modes ($A'(0) = 1$ for the odd ones). Properties of the first four

even neutral-wave solutions with the mode numbers $n = 0$-3 are illustrated in Figs. 2,3a-d. The computation based on Newton's search for the couple of real $\tilde{\alpha}, \tilde{c}$ for a given spanwise wavenumber $\tilde{\beta}$ starts at a suitably large $\tilde{\beta}$, where the initial guesses are made using the asymptotic behaviour (3.11). Marching along the $\tilde{\beta}$-axis backwards with a reasonably fine step (on several occasions as small as $-2 \cdot 10^{-3}$) we were then able to extend the neutral-wave parameters into the domain of smaller $\tilde{\beta}$, hence verifying the limit form as $\tilde{\beta} \to 0$ with the core of the amplitude centred around one of the two stationary points, in our case at $\zeta = 0$ with the limit values $\tilde{\alpha} = -0.2167, \tilde{c} = 0.6823$, or at $\zeta = \pi$ with $\tilde{\alpha} = 0.2589, \tilde{c} = 1.2134$ following from the conditions (3.17) with (4.2), (4.3). The limit values are also marked in Fig. 2.

The most peculiar feature of the solution is the continuation of the third mode, $n = 2$ in Fig. 2, towards the small- $\tilde{\beta}$ limit with the larger phase speed, with the core near $\zeta = \pi$, as opposed to the limit of the modes 0, 1, 3 centred at $\zeta = 0, 2\pi$; see also Figs. 3a-d. This is obviously a consequence of the complex coefficients in the Mathieu equation (4.2), cf. the case of real coefficients in Abramowitz & Stegun (1970). It was verified, by refining the ζ-grid and taking smaller steps in $\tilde{\beta}$, that modes 1 and 2 have no common points, although the paths of the two roots in $(\tilde{\alpha}, \tilde{c}, \tilde{\beta})$ space become very close when $\tilde{\beta} \approx 0.4$-$0.5$. The approach of the large-$\tilde{\beta}$ solutions in Figs. 3a-d to simple harmonics, the appearance of concentrated amplitudes at smaller $\tilde{\beta}$, and a fairly accurate reproduction of the limit values at $\tilde{\beta} = 0$ in Fig. 2, all this is in favourable agreement with the conclusions drawn in section 3 for a general smooth vortex field.

In the *second example* the curvature remains smooth across the boundary layer with, however, piecewise continuity along the span, thus providing a model of the three-dimensional velocity field with abrupt spanwise changes in the magnitude and/or direction of the streamwise vorticity. The curvature function is defined in this case by

$$K_1 = \Phi(\tilde{\zeta})(1 + Y^2)^{-1}, \tag{4.4}$$

with the new scaled spanwise variable $\tilde{\zeta} = \zeta \tilde{\beta}^{-1}$ introduced for convenience. The spanwise modulation of the vortex is taken in the form

$$\Phi(\tilde{\zeta}) = \Phi_+, \text{ if } 0 \leq \tilde{\zeta} < \tilde{\zeta}_0 \text{ and } \tilde{\zeta}_1 + \tilde{\zeta}_0 < \tilde{\zeta} \leq \tilde{\zeta}_1 + 2\tilde{\zeta}_0, \tag{4.5}$$

$$\Phi(\tilde{\zeta}) = -\Phi_-, \text{ if } \tilde{\zeta}_0 \leq \tilde{\zeta} \leq \tilde{\zeta}_1 + \tilde{\zeta}_0, \tag{4.6}$$

2

over the first period $0 \leq \tilde{\zeta} \leq \tilde{\zeta}_1 + 2\tilde{\zeta}_0$, with constant parameters $\tilde{\zeta}_0, \tilde{\zeta}_1, \Phi_\pm$. The amplitude equation rewrites then as

$$A_{\tilde{\zeta}\tilde{\zeta}} + \left[\tilde{\alpha} + (s_1 + is_2)\tilde{c} - s_3\pi(\pm\Phi_\pm)(\tilde{c}+i)^{-1}\right] A = 0, \qquad (4.7)$$

where the choice of the sign depends on the spanwise location in accordance with (4.5), (4.6) above. Periodic solutions for $A(\tilde{\zeta})$ are constructed explicitly using the continuity of A and $A_{\tilde{\zeta}}$ at the vortex discontinuities; this yields the dispersion relation

$$(m_1 + m_2)\left[\exp(2m_1\tilde{\zeta}_0) - \exp(-m_2\tilde{\zeta}_1)\right] = -(m_2 - m_1)\left[1 - \exp(2m_1\tilde{\zeta}_0 - m_2\tilde{\zeta}_1)\right]$$

$$(4.8)$$

for the even modes, and the same expression but with the opposite sign to the right-hand side for the odd ones. The wave parameters are contained in $m_{1,2}$ given by

$$m_{1,2} = \left[-\tilde{\alpha} - (s_1 + is_2)\tilde{c} + s_3\pi(\pm\Phi_\pm)(\tilde{c}+i)^{-1}\right]^{1/2}, \quad |\arg(m_{1,2})| < \pi/2. \quad (4.9)$$

The non-smoothness of the curvature distribution in this model has only minor effect on the properties of shorter-scale flows with small $\tilde{\zeta}_1 + 2\tilde{\zeta}_0$. Assuming that $\tilde{\zeta}_1 \to 0$ and the geometric ratio $2\tilde{\zeta}_0/\tilde{\zeta}_1$ is kept constant it then follows from (4.8), (4.9) that $\tilde{\alpha}, \tilde{c}$ are finite and related by means of the equation

$$\tilde{\alpha} + (s_1 + is_2)\tilde{c} + s_3\pi\tilde{q}(\tilde{c}+i)^{-1} = 0, \qquad (4.10)$$

in the limit for the first even mode, with the constant

$$\tilde{q} = (\tilde{\zeta}_1\Phi_- - 2\tilde{\zeta}_0\Phi_+)/(\tilde{\zeta}_1 + 2\tilde{\zeta}_0) \qquad (4.11)$$

being a characteristic of the total vorticity in the flow, cf. (3.13) with $n = 0$, $A_0^{(0)} = 1$. Separating of the real and imaginary parts yields

$$\tilde{\alpha} + s_1\tilde{c}_r - s_2\tilde{c}_i + \tilde{q}\tilde{c}_r[\tilde{c}_r^2 + (\tilde{c}_i + 1)^2]^{-1} = 0, \qquad (4.12)$$

$$s_1\tilde{c}_i + s_2\tilde{c}_r = \tilde{q}(\tilde{c}_i + 1)[\tilde{c}_r^2 + (\tilde{c}_i + 1)^2]^{-1}, \qquad (4.13)$$

in turn, and hence, for any fixed growth rate $\tilde{c}_i$, including $\tilde{c}_i = 0$, the phase speed $\tilde{c}_r$ and the wavenumber $\tilde{\alpha}$ are uniquely determined by (4.13), (4.12) respectively.

3

Provided that s_2 is positive (as in the computational example to be discussed shortly) instability corresponds to disturbances with shorter wavelength, on account of the limit relation

$$\tilde{c}_i = s_2 \tilde{\alpha}(s_1^2 + s_2^2)^{-1} + ..., \text{ as } \tilde{\alpha} \to \infty, \tag{4.14}$$

also stemming from (4.12), (4.13).

For even modes with higher numbers we write, in the same shorter-scale limit,

$$\tilde{\alpha} = 4n^2\pi^2(\tilde{\zeta}_1 + 2\tilde{\zeta}_0)^{-2} + \tilde{\alpha}_1 + ..., \ (\tilde{\alpha}_1, \tilde{c}) = O(1), n = 1, 2, ..., \tag{4.15}$$

and derive, on substituting into (4.8), (4.9), the limit relation between $\tilde{\alpha}_1$ and $\tilde{c}$ in the following form

$$\tilde{\alpha}_1 + (s_1 + is_2)\tilde{c} + s_3(\tilde{c} + i)^{-1}\left[\pi\tilde{q} - (2n)^{-1}(\Phi_+ + \Phi_-)\sin\left[4n\pi\tilde{\zeta}_0/(\tilde{\zeta}_1 + 2\tilde{\zeta}_0)\right]\right] = 0, \tag{4.16}$$

which is also a consequence of (3.13) in section 3.

The larger-scale limit behaviour of the roots of (4.8), (4.9) is noticeably different from the stationary-point limit of the previous example because reduction to the Weber equation locally is not possible now, yet there exist certain similarities between the two problems. The dispersion relation (4.8) suggests that both $\tilde{\alpha}$ and $\tilde{c}$ are $O(1)$ when $\tilde{\zeta}_1, \tilde{\zeta}_0 \to \infty$, so that either $Real(m_1) > 0$ and then $\exp(-m_2\tilde{\zeta}_1) \to -1$ in the limit, or, alternatively, $Real(m_2) > 0$ and $\exp(2m_1\tilde{\zeta}_0) \to -1$. This yields two families of solutions with the behaviour

$$-\tilde{\alpha}_1 - (s_1 + is_2)\tilde{c} + s_3\pi(\tilde{c} + i)^{-1}\Phi_+ = (2n + 1)^2\pi^2(2\tilde{\zeta}_0)^{-2} + ..., \tag{4.17}$$

$$-\tilde{\alpha}_1 - (s_1 + is_2)\tilde{c} - s_3\pi(\tilde{c} + i)^{-1}\Phi_- = (2n + 1)^2\pi^2\tilde{\zeta}_1^{-2} + ..., \tag{4.18}$$

as $(\tilde{\zeta}_0, \tilde{\zeta}_1) \to \infty$, with integer n. It can be shown by taking the limit solutions of the equation (4.7) that the leading-order amplitude distribution corresponding to (4.17) has the oscillatory form $A = \cos[|m_1|\ (\tilde{\zeta} - N(\tilde{\zeta}_1 + 2\tilde{\zeta}_0))]$ in the intervals of length $2\tilde{\zeta}_0$ centred at the end-points of the periods $\tilde{\zeta} = N(\tilde{\zeta}_1 + 2\tilde{\zeta}_0), N = 0, \pm 1, \pm 2, ...$. In the gaps between the ranges of oscillations the amplitude $|A|$ turns out to be exponentially small so that (4.17) is equivalent to the requirement of having the nodes of the oscillatory functions at the junction points, or $\cos(|m_1| \tilde{\zeta}_0) = 0$, at the main order. Similarly, the set of roots (4.18) corresponds to an

4

exponentially weak wave when $|\tilde{\zeta} - N(\tilde{\zeta}_1 + 2\tilde{\zeta}_0)| < \tilde{\zeta}_0$ and spanwise oscillations in the amplitude in the remaining part of the flow. So, by analogy to the previous example, the larger-scale waves are dominant near the extremum points in the vortex curvature spanwise, cf. the second condition (3.17) for a smooth vortex.

For the neutral disturbances the relations (4.17), (4.18) predict two limit values of the phase speed given by the roots of

$$s_2 \tilde{c} \pm \pi s_3 (\tilde{c}^2 + 1) \Phi_\pm = 0, \qquad (4.19)$$

with the limit wavenumbers provided by the real part of (4.17), (4.18).

In Figs. 4a-c we plot the neutral wavenumber $\tilde{\alpha}$ against the length parameter $\tilde{\zeta}_1$ for the first six even modes computed from (4.8), (4.9) for the case $\Phi_+ = s_{1-3} = 1$. The spanwise intervals of constant curvature were taken to be of equal length, $2\tilde{\zeta}_0 = \tilde{\zeta}_1$, whereas the period-averaged vorticity varies in accordance with the values $\Phi_- = 0; 0.8; 1$. As the quantity $\Phi_+ - \Phi_-$ decreases from 1 to 0 the well-behaved pattern of the neutral curves in Fig. 4a becomes nonmonotonic for the modes $n = 1, 3, 5$ (Fig. 4b) and eventually splits into almost disconnected loops formed by the branches with odd and even numbers, Fig. 4c. The high symmetry in the flow in the latter case introduces several interesting features in the solution. So, the phase speed turns out to be zero on branches 0-5; this property follows from (4.8), (4.9) and also reflects itself in the limit solutions (4.13), (4.16). Along the branches denoted as 0'-5' the phase speed is non-zero in general, see e.g. the limit relations (4.19), although our computations point to the existence of a common point with equal $\tilde{\alpha}$ and $\tilde{c} = 0$ (dots in Fig. 4c) for each pair of the intersecting loops. If we add the third coordinate $\tilde{c}_i$ to the axes $\tilde{\zeta}_1, \tilde{\alpha}$ then the solutions of (4.8), (4.9) can be interpreted as an infinite sequence of surfaces which cross the plane $\tilde{c}_i = 0$ along the neutral curves. The mode coupling then turns out to be structurally unstable to small changes in the growth rates, as illustrated in Fig. 5 which also suggests a saddle point in the shape of the instability surfaces in the $\tilde{\zeta}_1, \tilde{\alpha}, \tilde{c}_i$ space near the common points.

In our *third example* the vortex curvature has discontinuities along the span as before and, in addition, jumps across the layer, specifically we define

$$K_1 = \Phi(\tilde{\zeta}) \text{ if } Y_0 \leq Y \leq Y_1, \qquad (4.20)$$

and $K_1 \equiv 0$ if $Y > Y_1$ or $Y < Y_0$, where $Y_{0,1}$ are constants and $\Phi(\tilde{\zeta})$ is given by (4.5), (4.6). This model has certain although fairly loose similarities with the

5

concentrated nonlinear Görtler vortices of Hall & Lakin (1988). The dispersion relation for the even modes is again of the form (4.8) but with

$$m_{1,2} = \{-\tilde{\alpha} - (s_1 + is_2)\tilde{c} \mp s_3\Phi_\pm [\ln[(Y_1 - \tilde{c})/(\tilde{c} - Y_0)] + i\pi]\}^{1/2}, \quad |\arg(m_{1,2})| < \pi/2. \tag{4.21}$$

in the case of neutral disturbances. The solution discussed below turns out to be such that the phase speed of the disturbance remains bounded in the range $Y_0 < \tilde{c} < Y_1$, where the argument of the logarithm in (4.21) is positive.

The neutral wavenumbers for the first several modes are shown in Fig. 6a. The short-scale branches of the neutral curves in that figure originating at a finite limit wavenumber for the first mode and going upwards to infinity for the higher modes are qualitatively similar to those in the previous examples, cf. Figs. 2,4, and the corresponding asymptotic formulae can be found readily using the procedure which had earlier led to (4.10), (4.16). The most striking property of the current solution, compared to the other examples, is the reversal of the neutral curves into the region of shorter spanwise scales after reaching a certain threshold, with a trend to an unbounded growth in the magnitude of the wavenumber as the flow period decreases. The plots of the neutral curves in the plane of the parameters $\tilde{c}, \tilde{\alpha}$ in Fig. 6b indicate a fast approach of the phase speed to one of the two limit values $\tilde{c} = \pm 2$, with the location of the critical layer being shifted towards the normal boundaries of the vortex at $Y = Y_{0,1} = \pm 2$. Hence the reversal of the plots in Fig. 6a and consequently non-existence of larger-scale neutral modes is due to the logarithmic singularities in the integral term in the equation (3.8).

The asymptotic form of the reversed branches can be found as follows. Suppose that $2\tilde{\zeta}_0 = \tilde{\zeta}_1 = \epsilon \to 0$, and expand $m_{1,2}$ in (4.8) in the form

$$m_{1,2} = \epsilon L_{1,2} + \epsilon l_{1,2} + ..., \quad \text{as } \epsilon \to 0. \tag{4.22}$$

Substitution into (4.8) yields

$$(L_1 + L_2)[\exp(L_1) - \exp(-L_2)] = -(L_2 - L_1)[1 - \exp(L_1 - L_2)], \tag{4.23}$$

$$l_1[\exp(L_1) - \exp(-L_2) + (L_1 + L_2)\exp(L_1) - 1 + (1 + L_1 - L_2)\exp(L_1 - L_2)] =$$
$$-l_2[\exp(L_1) - \exp(-L_2) + (L_1 + L_2)\exp(-L_2) + 1 - (1 + L_1 - L_2)\exp(L_1 - L_2)], \tag{4.24}$$

in the first two approximations respectively. The accompanying expansions for the wave parameters are

$$\tilde{\alpha} = \epsilon^{-2}\tilde{\alpha}_0 + \tilde{\alpha}_1 + ..., \tilde{c} = \tilde{c}_1 + ..., \ln\left[(Y_1 - \tilde{c})/(\tilde{c} - Y_0)\right] = \epsilon^{-2}\kappa_0 + \kappa_1 + ..., \quad (4.25)$$

where the leading-order phase speed $\tilde{c}_1$ will be subsequently equal to 2 or -2, depending on the branch of the solution, and κ_0, κ_1 are real. It then follows from (4.21), (4.22), (4.25) that

$$L_{1,2}^2 = -\tilde{\alpha}_0 \mp s_3\Phi_\pm\kappa_0, \quad (4.26)$$

$$2l_{1,2}L_{1,2} = -\tilde{\alpha}_1 - (s_1 + is_2)\tilde{c}_1 \mp s_3\Phi_\pm(\kappa_1 + i\pi). \quad (4.27)$$

The important consequence of (4.23) with (4.26) is that depending on the signs of $\tilde{\alpha}_0, \kappa_0$ one of the two quantities $L_{1,2}$ must be real and the other purely imaginary so that making the substitution

$$L_1 = 2\rho\cos\varphi, L_2 = i2\rho\sin\varphi \quad (4.28)$$

for real L_1 or, alternatively,

$$L_1 = i2\rho\sin\varphi, L_2 = 2\rho\cos\varphi \quad (4.29)$$

for real L_2, the equation (4.23) reduces to

$$\exp(\rho\cos\varphi)\cos(\varphi + \rho\sin\varphi) = \exp(-\rho\cos\varphi)\cos(\varphi - \rho\sin\varphi), \quad (4.30)$$

whereas (4.24) indicates that the ratio l_1/l_2 is then purely imaginary,

$$l_1/l_2 = iQ(\rho, \varphi), \quad (4.31)$$

say, with the real Q given by

$$Q = -\frac{(e^R + e^{-R})\sin(\rho\sin\varphi) + \rho e^{-R}\sin(\varphi - \rho\sin\varphi) + \rho e^R\sin(\varphi + \rho\sin\varphi)}{(e^R + e^{-R})\cos(\rho\sin\varphi) + 2\rho e^R\cos(\varphi + \rho\sin\varphi)},$$
$$(4.32)$$

$$Q = \frac{(e^R + e^{-R})\cos(\rho\sin\varphi) + 2\rho e^{-R}\cos(\varphi - \rho\sin\varphi)}{(e^R + e^{-R})\sin(\rho\sin\varphi) + \rho e^{-R}\sin(\varphi - \rho\sin\varphi) + \rho e^R\sin(\varphi + \rho\sin\varphi)},$$
$$(4.33)$$

for the cases (4.28), (4.29) respectively, where

$$R = \rho\cos\varphi. \quad (4.34)$$

7

Denoting also

$$L_1/L_2 = -iP, \tag{4.35}$$

with P being a real function of φ, the ratio l_1/l_2 can be expressed in terms of the wave parameters contained in (4.27), leading eventually to the relation

$$P(\rho, \varphi)Q(\rho, \varphi) = (\tilde{c}_1 s_2 + s_3 \Phi_+ \pi)/(\tilde{c}_1 s_2 - s_3 \Phi_- \pi). \tag{4.36}$$

In order to establish the leading term $\tilde{\alpha}_0$ in the wavenumber expansion in (4.25) we first choose the limit value of the phase speed, $\tilde{c}_1 = 2$ for instance, and then, given the values of the other parameters on the right in (4.36), resolve the system of two equations (4.30), (4.36) with respect to ρ, φ, using (4.35) and either (4.28) or (4.29). The required value $\tilde{\alpha}_0$ follows then eliminating κ_0 between the two relations (4.26) in the form

$$\tilde{\alpha}_0 = -(L_1^2 \Phi_- + L_2^2 \Phi_+)/(\Phi_+ + \Phi_-), \tag{4.37}$$

where (4.28), (4.29) should be used again to evaluate $L_{1,2}$. An example of computation is summarised in Fig. 7 and below. The solid lines in the upper part of Fig. 7 represent solutions of (4.30) for φ as a function of ρ. The required branches form a discrete set $\varphi_n(\rho)$ with the limit properties

$$\varphi_n = (\frac{1}{2} + n)\pi\rho^{-1} + ..., \text{ as } \rho \to \infty, n = 0, \pm 1, \pm 2, ...; \tag{4.38}$$

$$\varphi_0 \to \pi/4 \text{ as } \rho \to 0; \tag{4.39}$$

$$\varphi_n \to sgn(n)(\frac{1}{2}\pi - 0) \text{ as } \rho \to n\pi + 0, n \neq 0. \tag{4.40}$$

The lower part of Fig. 7 contains plots of the function $P \cdot Q$ computed along the branches $\varphi_n(\rho), n = 0\text{-}3$ (negative n do not add new solutions of the full problem eventually). The solid curves correspond to real L_1, dashes are used for the case of real L_2. The right-hand side in (4.36) is equal to $(P \cdot Q)_1 = -0.2529$ when $\tilde{c}_1 = -2$ and $(P \cdot Q)_2 = -10.0172$ when $\tilde{c}_1 = 2$, using the values $\Phi_+ = 1$, $\Phi_- = 0.8, s_{1-3} = 1$, as in the computation for Figs. 6a,b. Hence the sequence of solutions (ρ, φ) arises at intersections of the plots for $P \cdot Q$ against ρ with the

8

horizontal lines $P \cdot Q = (P \cdot Q)_{1,2}$. This produces for the case $\tilde{c}_1 = -2$ the values $(\rho, \varphi) = (1.52, 0.612), (4.5, 0.977), (7.4, 1.137)$, and the corresponding wavenumber coefficients $\tilde{\alpha}_0 = -2.08, 10.62, 58.65$ approximately . When $\tilde{c}_1 = 2$, we obtain $(\rho, \varphi) = (2.22, 0.495), (5.77, 0.754), (8.96, 0.892)$, and then $\tilde{\alpha}_0 = -4.30, 3.18, 57.74$. In agreement with the trends in Fig. 6a, the two sequences start with negative $\tilde{\alpha}_0$, therefore $\tilde{\alpha} \to -\infty$ in the short-scale limit for the first two branches after reversal. By contrast, $\tilde{\alpha}_0$ is positive and $\tilde{\alpha} \to +\infty$ for higher modes. Note also the much faster, exponential, approach to the limit implied in the phase-speed expansion in (4.25) compared to the slower, algebraic, behaviour of the wavenumber, in qualitative agreement with the $\tilde{c}$-$\tilde{\alpha}$ plots in Fig. 6b.

Captions for figures.

Figure 1. a, the sketch illustrates the typical scales of a longitudinal vortex flow implied in the derivation of the inviscid instability equation (1.4); b, the streamwise velocity profiles shown qualitatively for the case of a weak vortex concentrated at the inflexion point y_c in the basic planar boundary layer, the scaled thickness of the vortex ε serves as the small parameter in the perturbation analysis in sections 2,3.

Figure 2. Neutral parameters plotted against the spanwise wavenumber $\tilde{\beta}$, from numerical solution of (4.2), (4.3) with $s_1 = s_3 = 1, s_2 = -1, \mu = 2/\pi, \nu = -1/\pi$, for the first four even modes of wave disturbances; — , the phase speed $\tilde{c}$; - - - , the wavenumber $\tilde{\alpha}/5$; the values $n = 0\text{-}3$ refer to the mode number. Crosses correspond to the stationary-point limit values $\tilde{c} = 0.6823, \tilde{\alpha} = -0.6823$ and $\tilde{c} = 1.2134, \tilde{\alpha} = 0.2589$.

Figure 3. The absolute value (solid) and the real part (dashes) of the amplitude function A plotted against the scaled spanwise variable $\hat{\zeta} = \zeta/(2\pi)$ for various $\tilde{\beta}$, from computations for figure 2. The solution functions are scaled to have a unit maximum modulus over the period; figs. a-d correspond to mode numbers 0-3 respectively; the values of $\tilde{\beta}$ are indicated at the plots; a,b, the amplitude function shown for the first period; c,d, plots for small and large $\tilde{\beta}$ are shown on separate half-periods.

Figure 4. The neutral wavenumber $\tilde{\alpha}$ plotted against the spanwise length parameter $\tilde{\zeta}_1 (=\text{half-length of the period})$ for the second model flow with the dispersion relation (4.8), (4.9); even modes with $s_{1-3} = \Phi_+ = 1$ and a, $\Phi_- = 0$; b,

9

$\Phi_- = 0.8$; c, $\Phi_- = 1$; the mode numbers $n = 0\text{-}5$ are shown in the figures. The mode splitting in the case c results in reconnections of the branches 0 and 1, 0′ and 1′, etc., with the dots indicating the location of the mode intersections.

Figure 5. Contours of constant growth rate in the plane $\tilde{\zeta}_1, \tilde{\alpha}$ near the neutral mode intersection point S; model flow (4.8), (4.9) with $s_{1-3} = \Phi_\pm = 1$; $0, 1, 0', 1'$, the neutral waves; I, growth rate $\tilde{c}_i = 0.01$; II, $\tilde{c}_i = 0.05$.

Figure 6. a, the neutral wavenumber of the dispersion relation (4.8), (4.21) plotted against the length parameter $\tilde{\zeta}_1$ for the case $2\tilde{\zeta}_0 = \tilde{\zeta}_1, s_{1-3} = \Phi_+ = 1, \Phi_- = 0.8$; the mode numbers are indicated at the plots. b, the neutral-wave phase speed against the wavenumber with varying $\tilde{\zeta}_1$ for the modes in figure a.

Figure 7. Plots of the solution of (4.30), $\varphi_n(\rho)$, and the function $P(\rho, \varphi)Q(\rho, \varphi)$ defined by (4.35), (4.28), (4.32) for the solid curves and by (4.35), (4.29), (4.43) for the dashed curves.
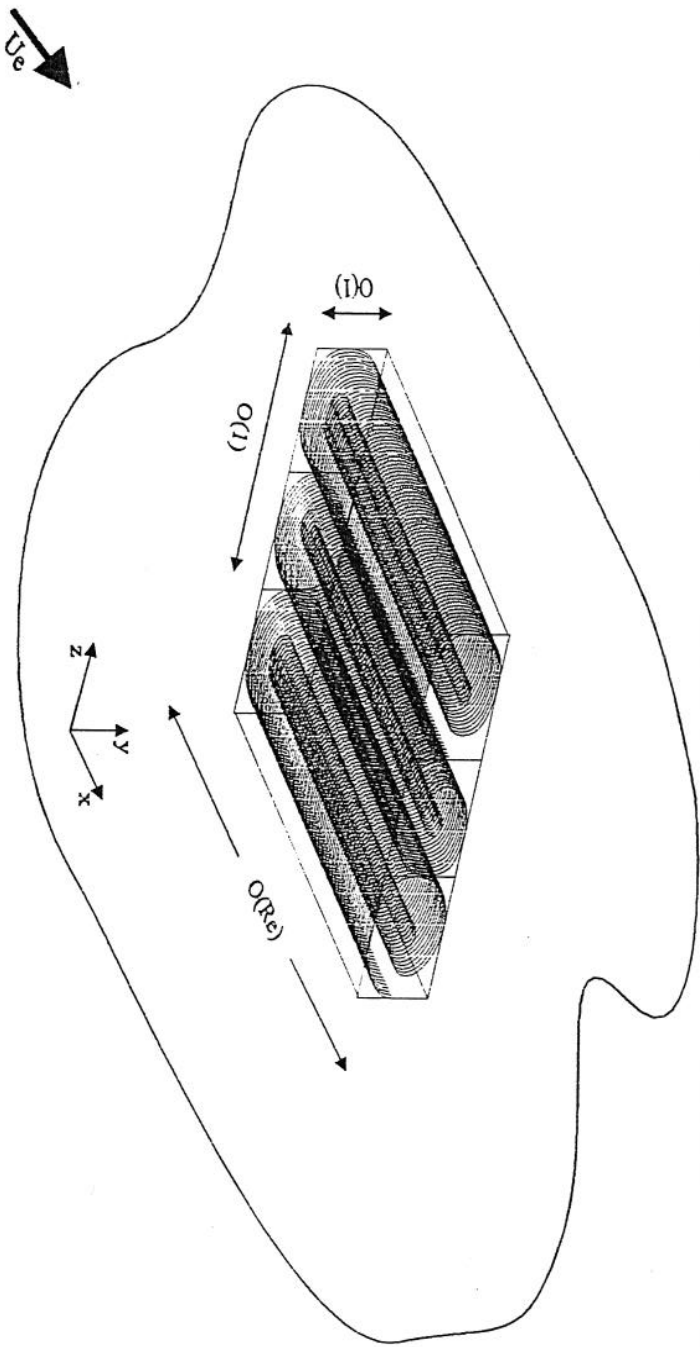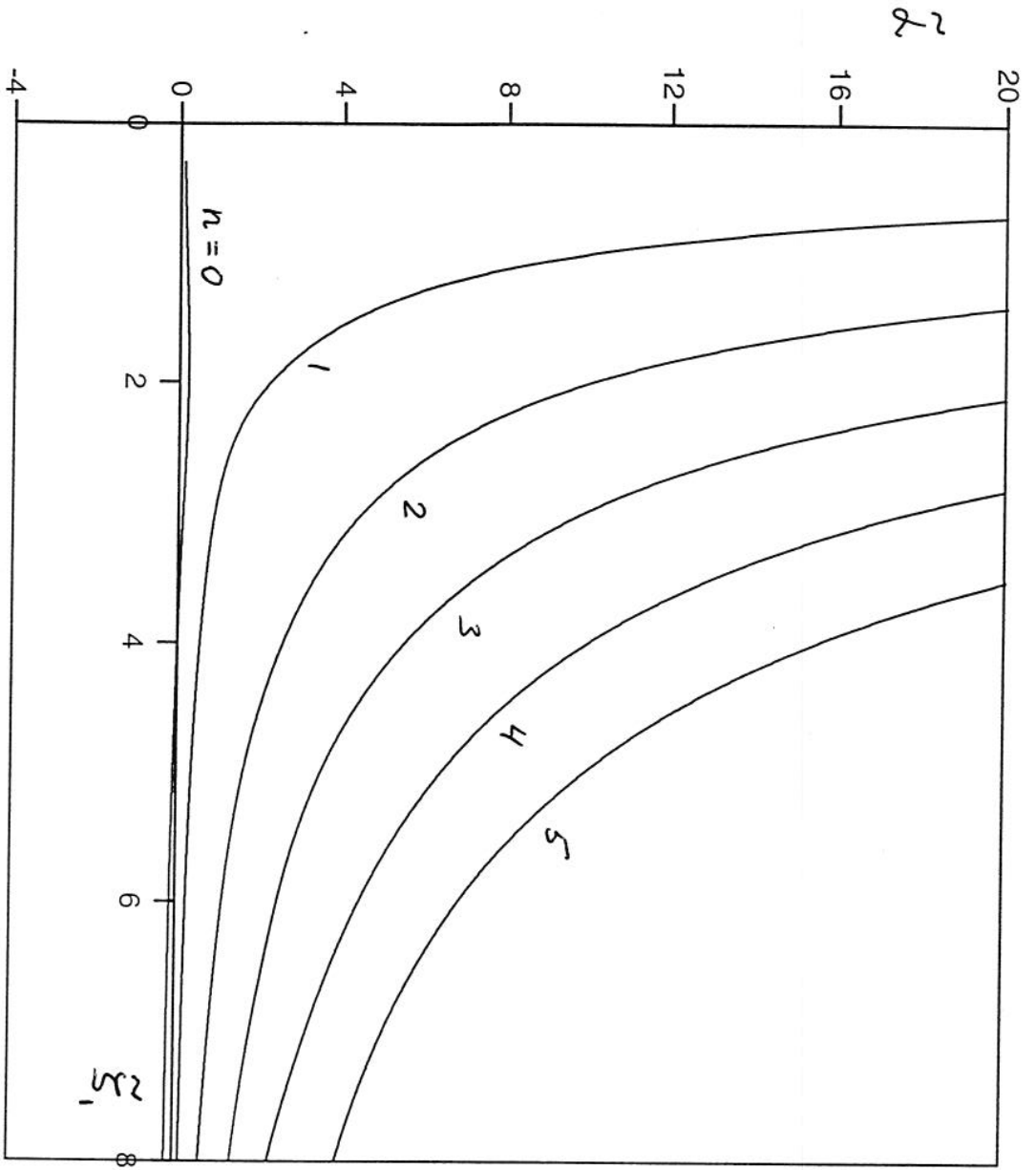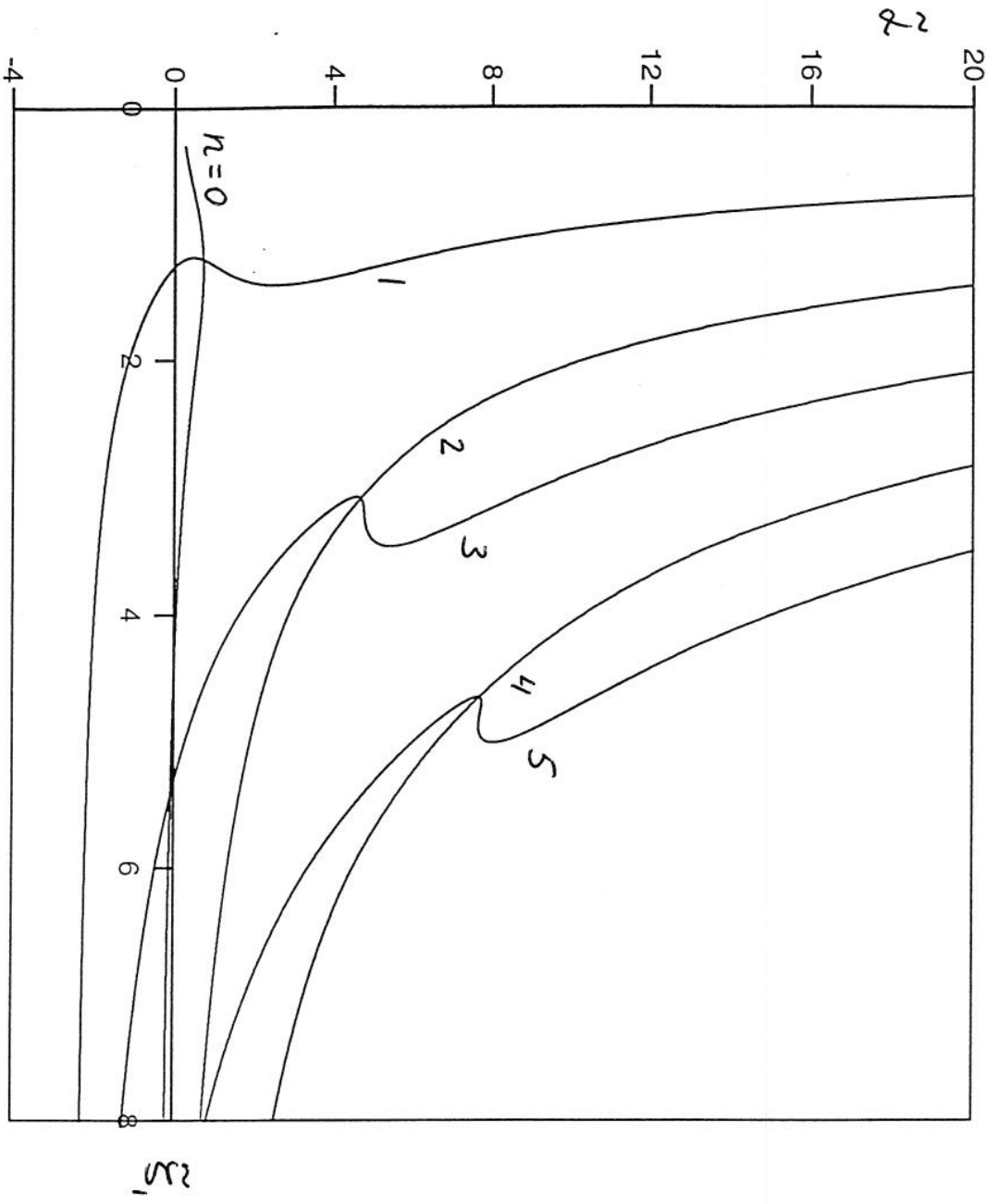
Figure 1a
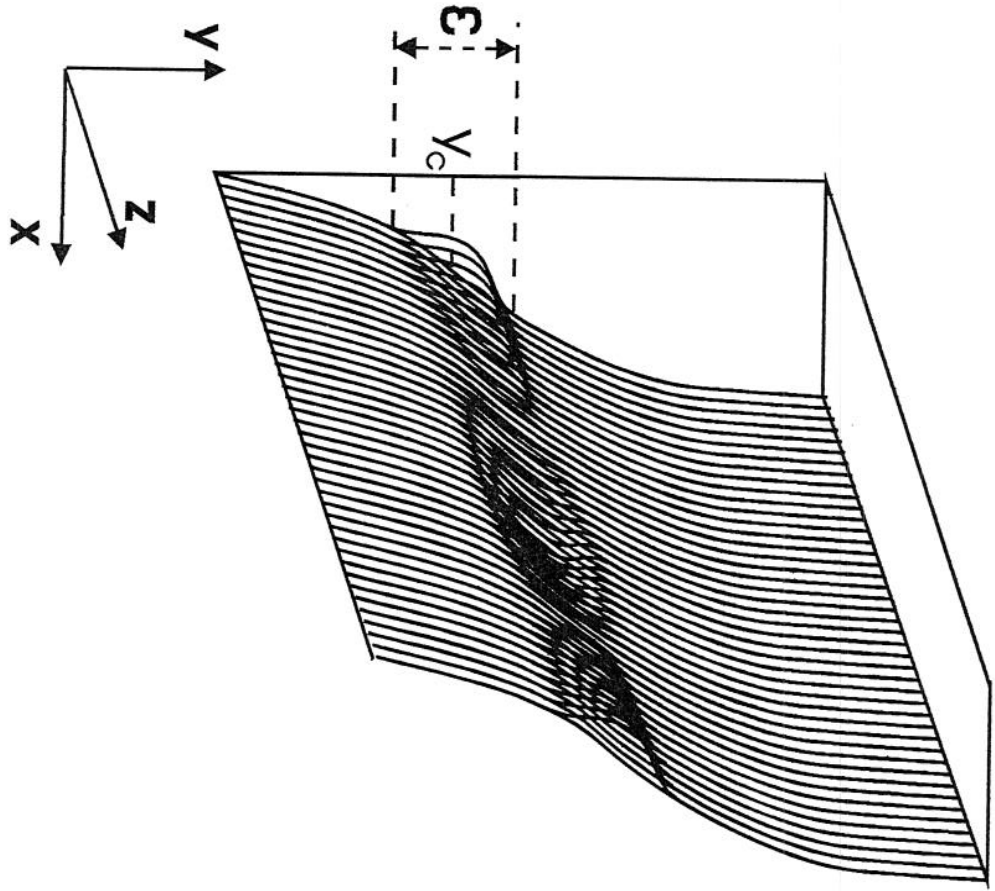
Figure 1b
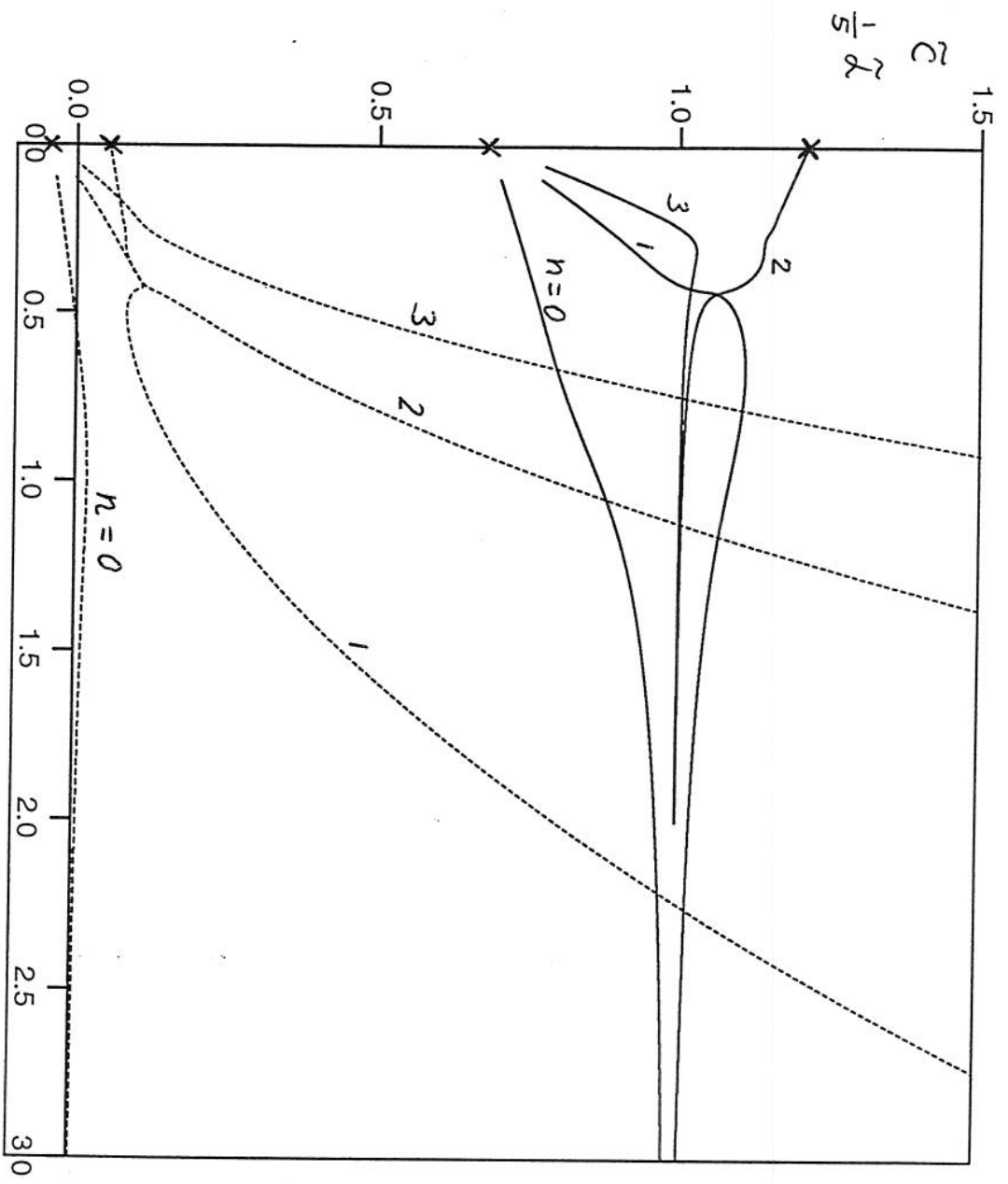
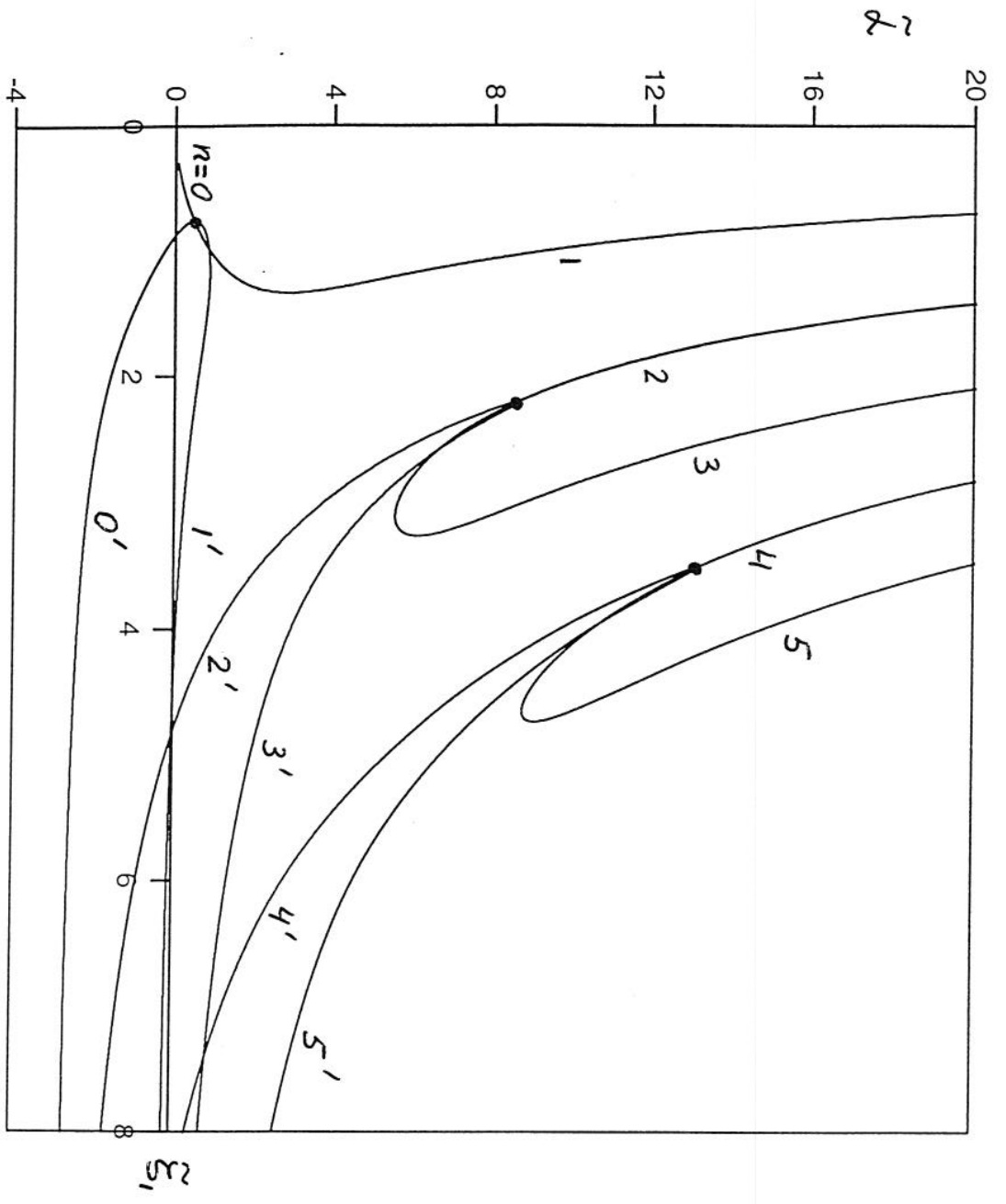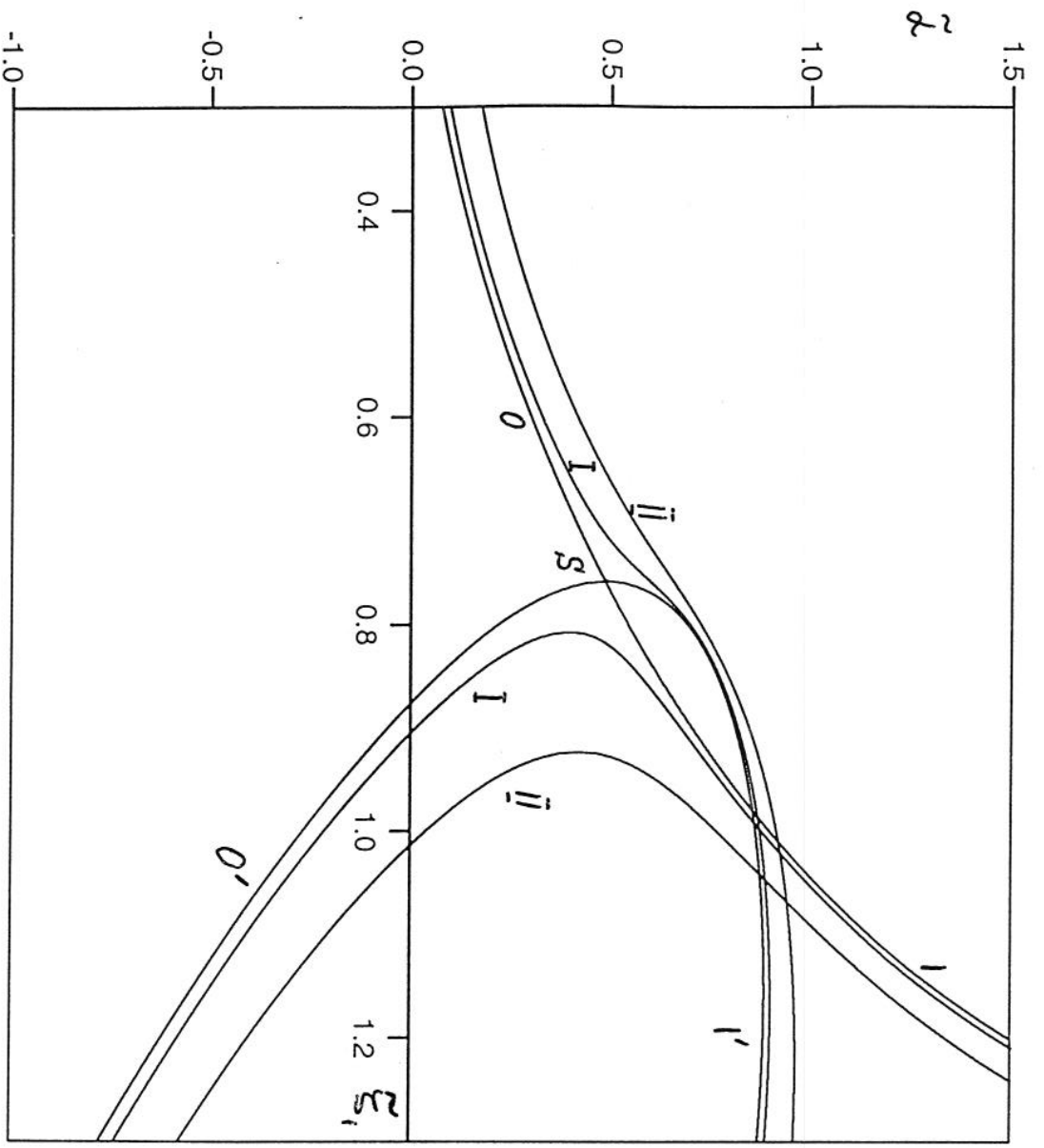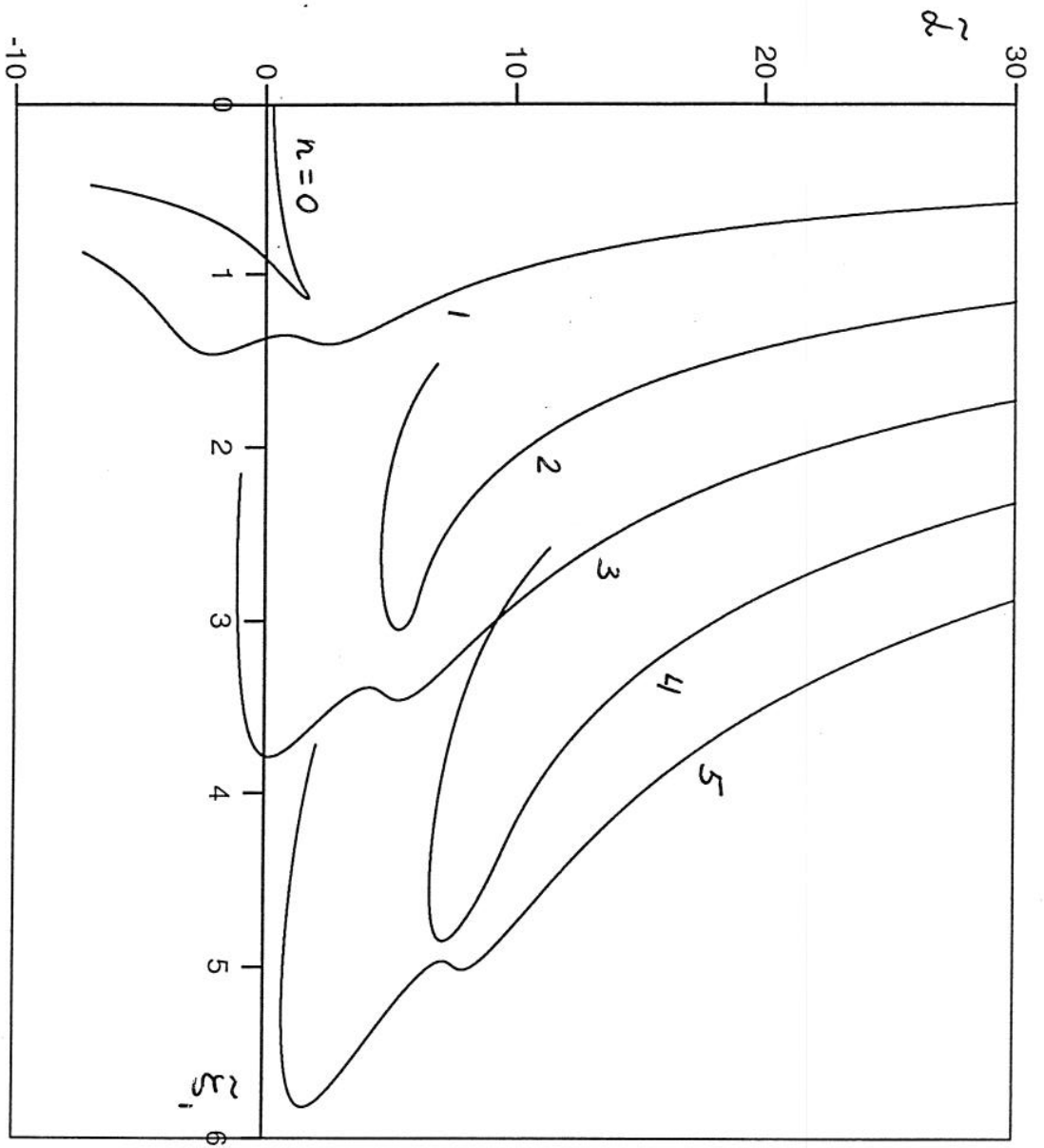Figure 2
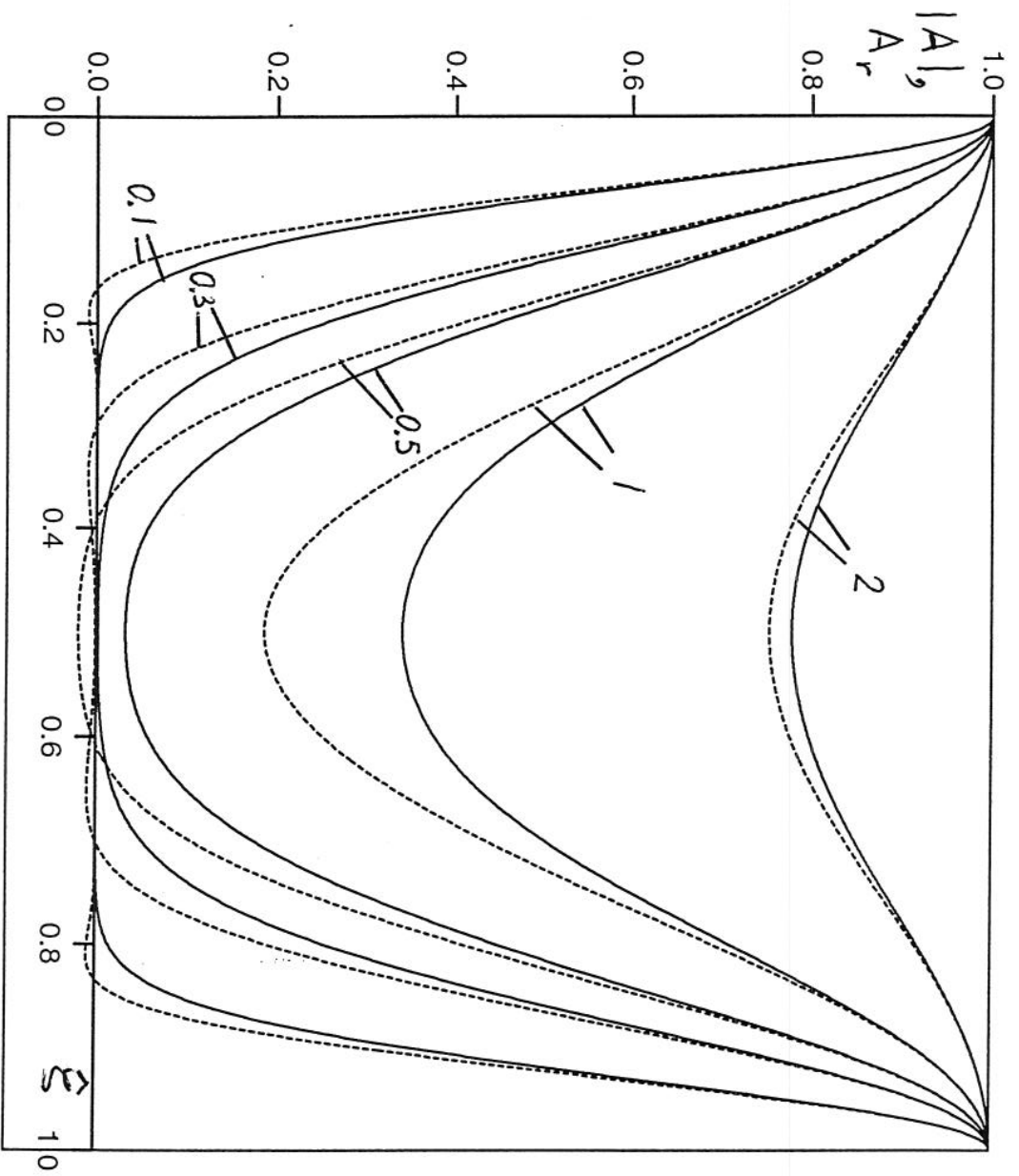
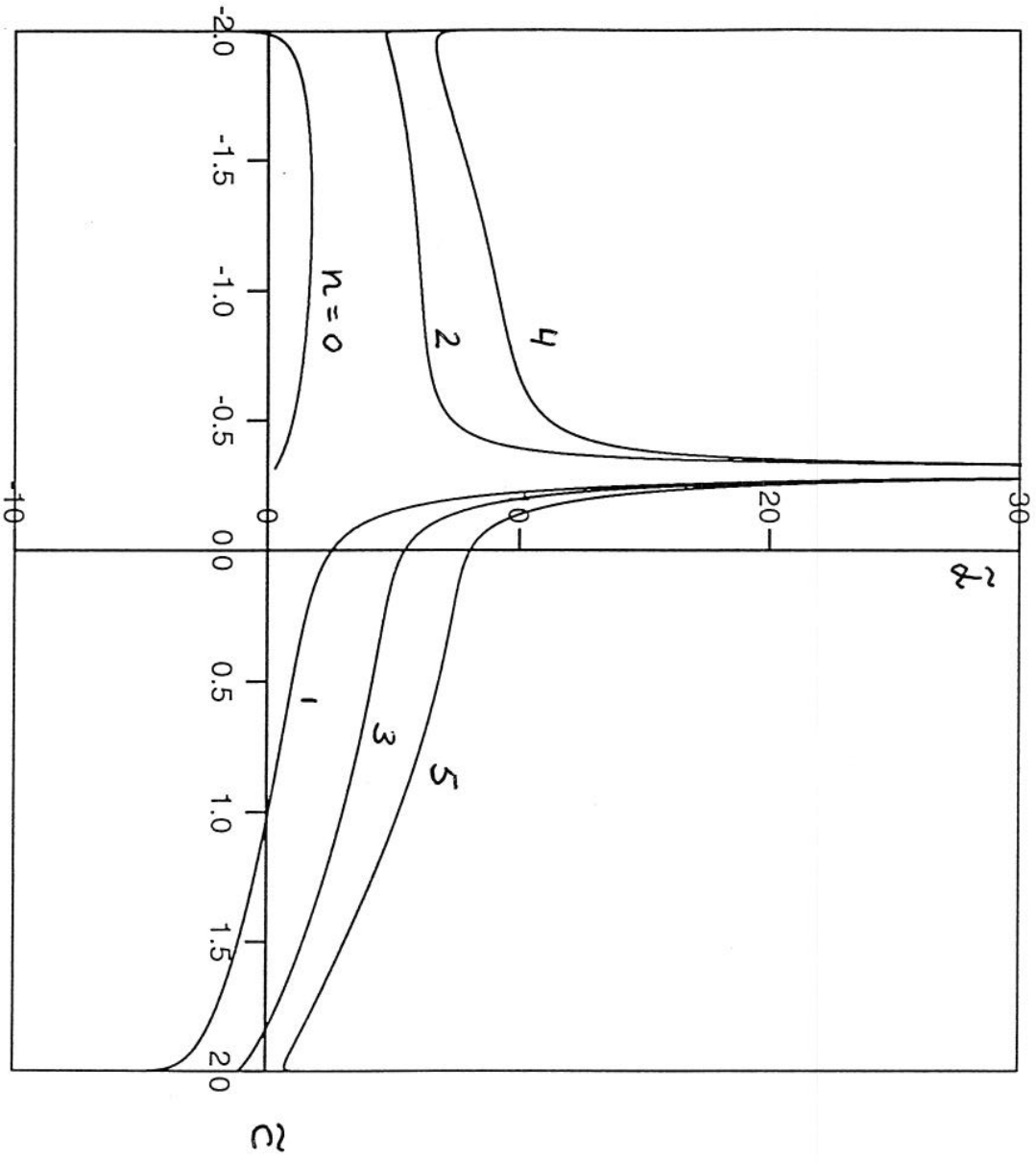Figure 3a
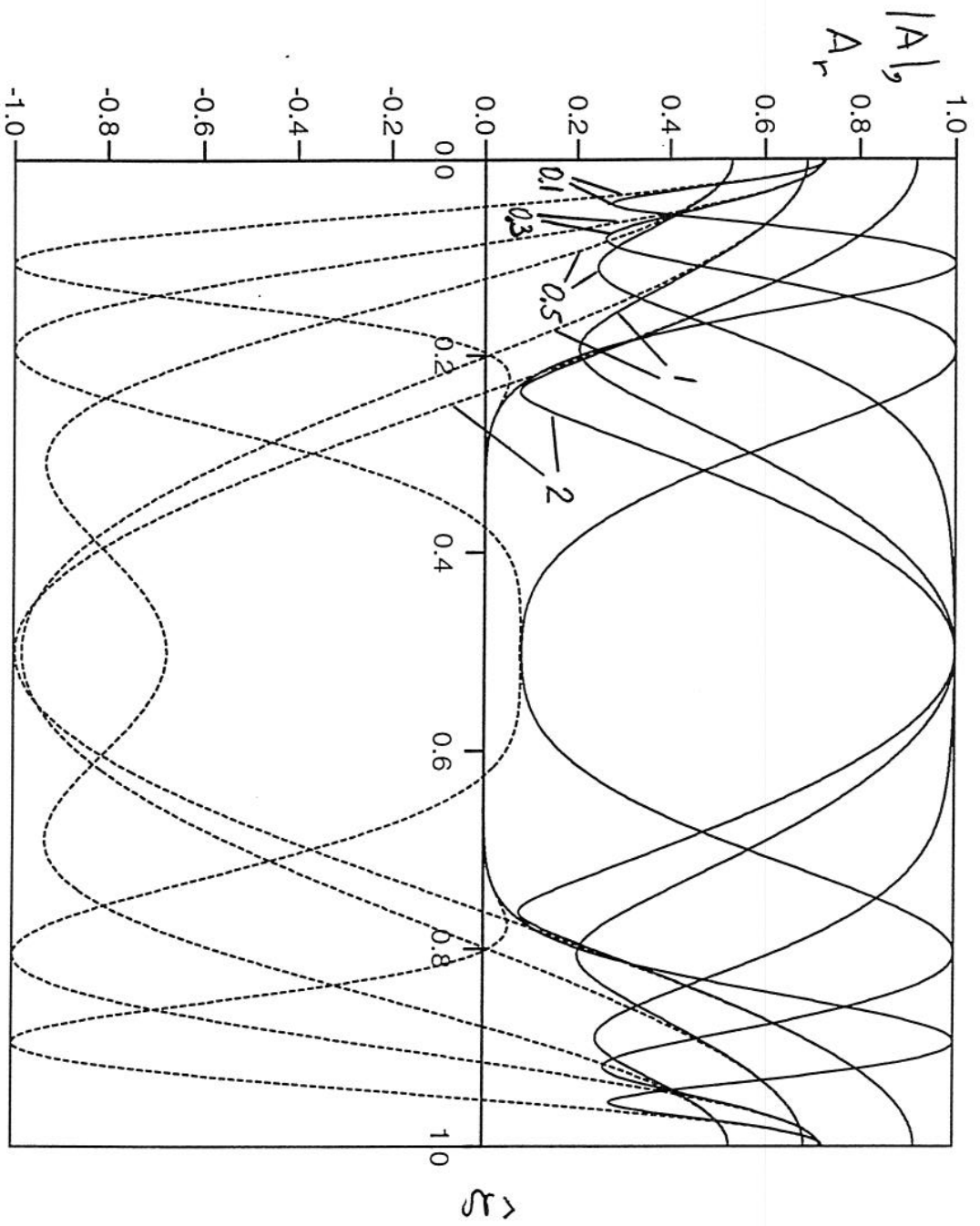
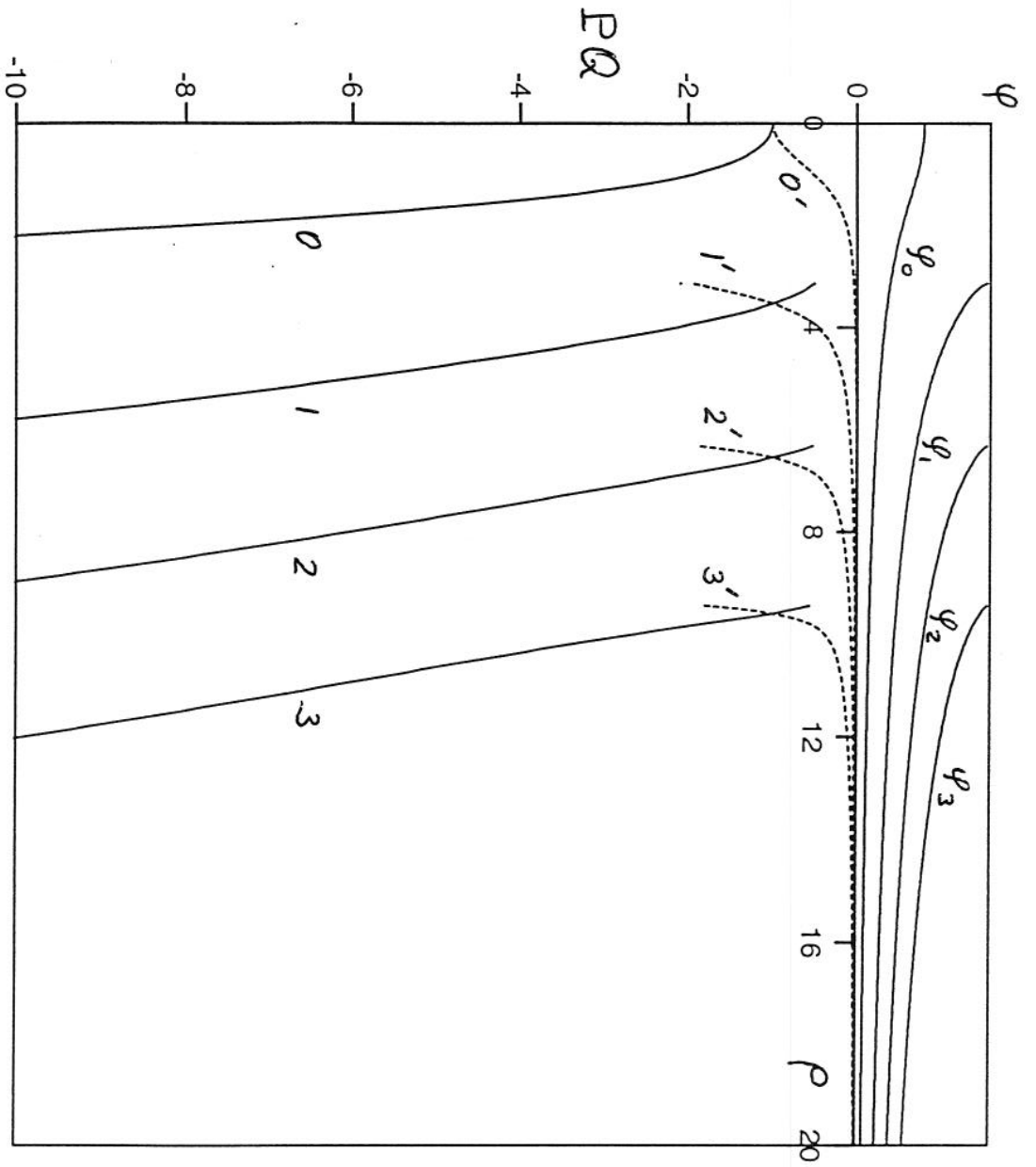Figure 3b
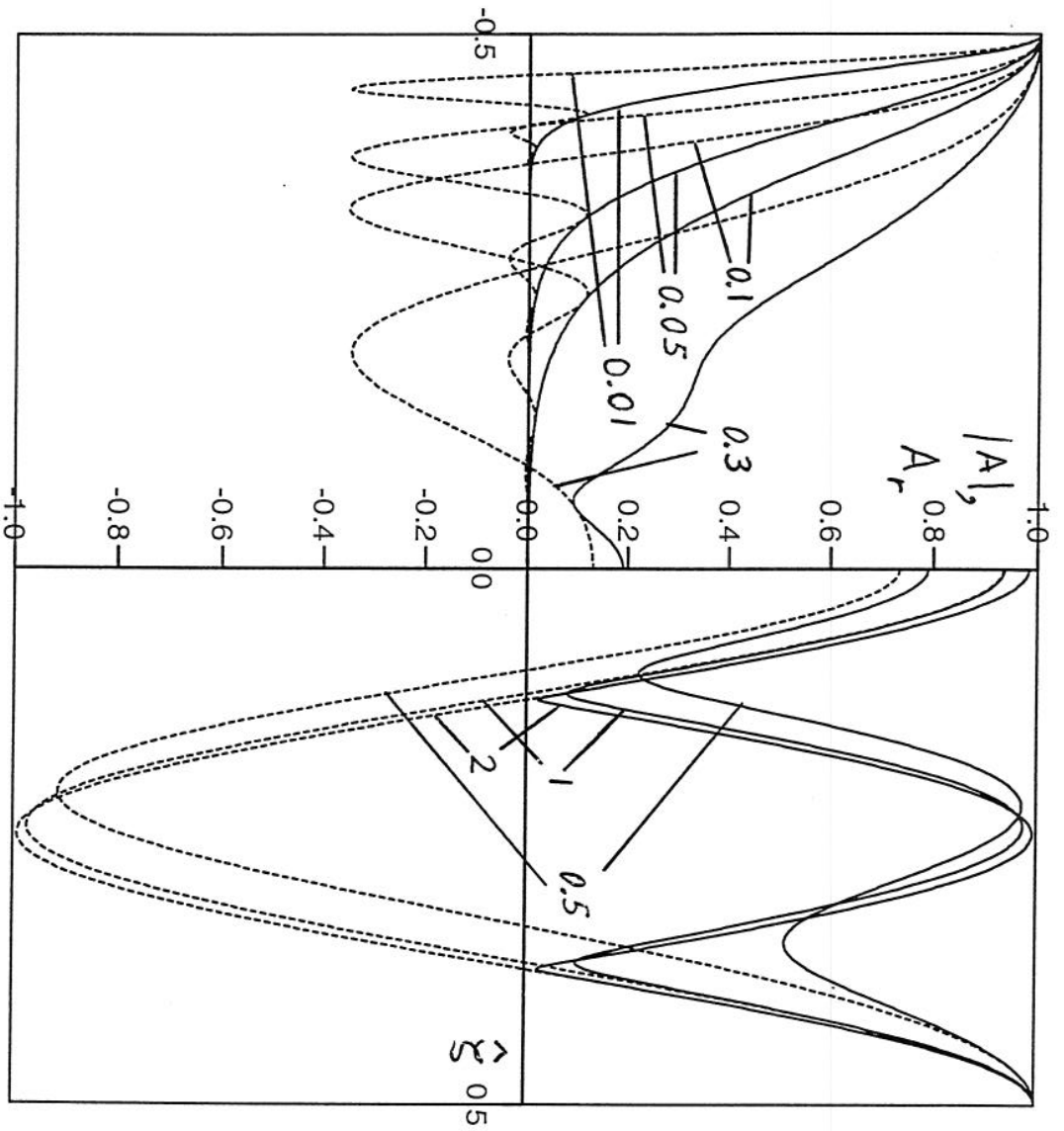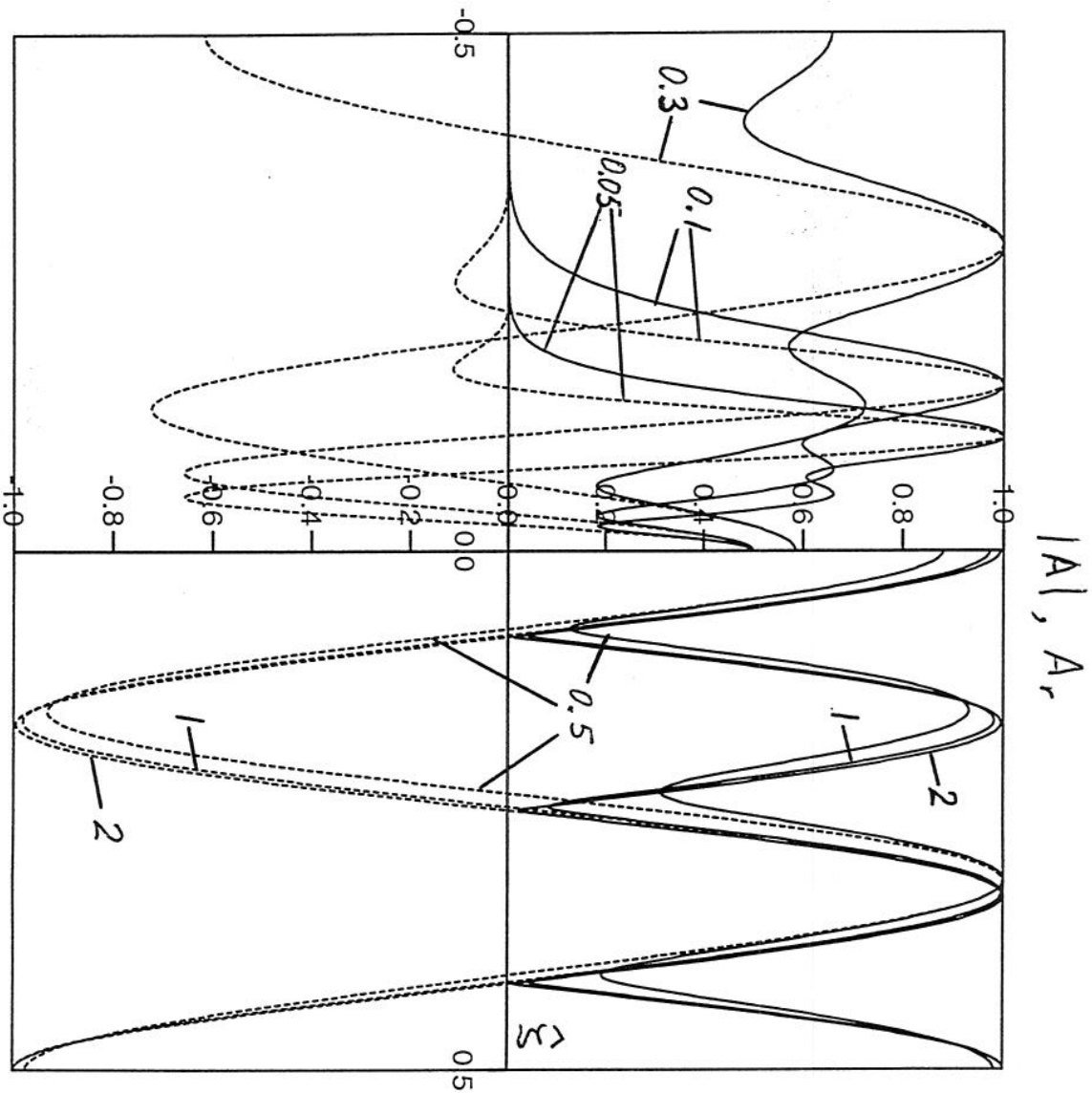
Figure 3c

Figure 3d

Figure 4a

Figure 4 b

Figure 4c

Figure 5

Figure 6a

Figure 6b

Figure 7